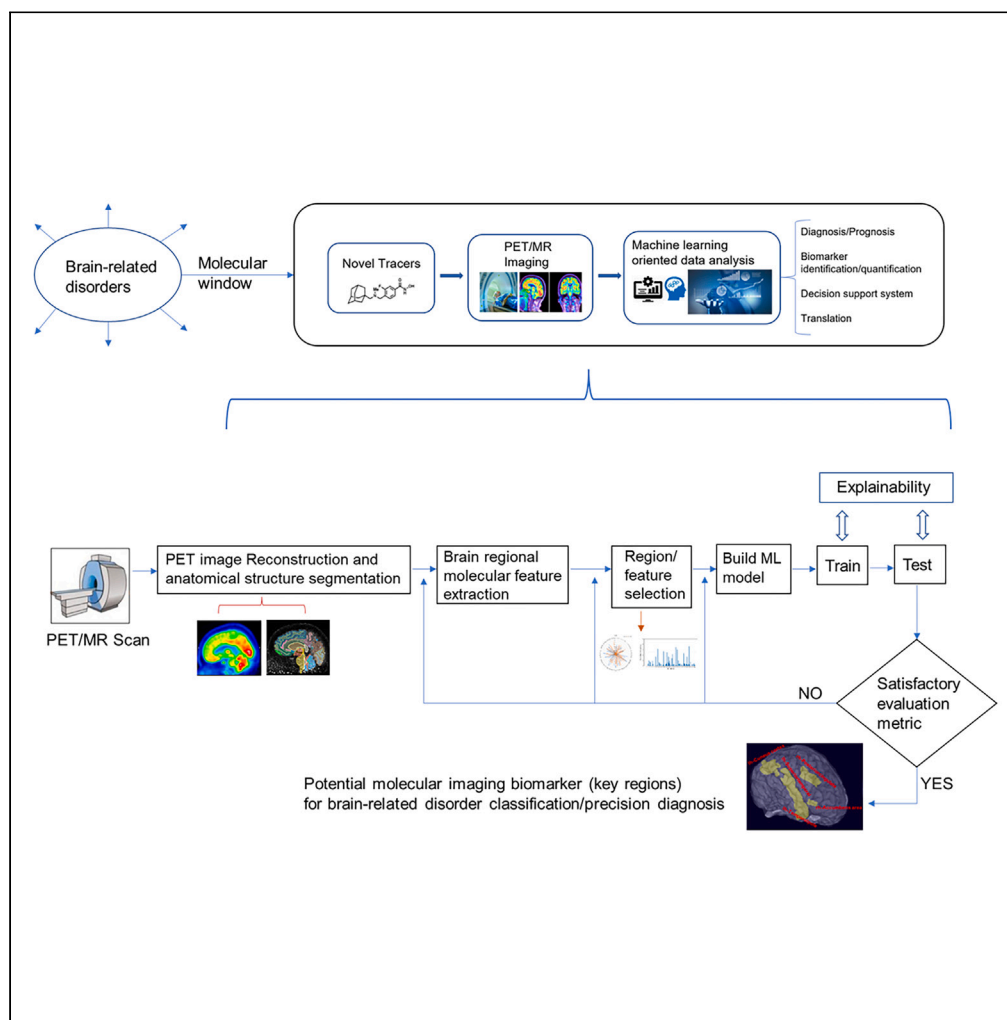**Article**

Toward AI-driven neuroepigenetic imaging biomarker for alcohol use disorder: A proof-of-concept study

Tewodros
Mulugeta Dagnew,
Chieh-En J. Tseng,
Chi-Hyeon Yoo, ...,
Jacob M. Hooker,
Roger D. Weiss,
Changning Wang

rweiss@mclean.harvard.edu
(R.D.W.)
cwang15@mgh.harvard.edu
(C.W.)

Highlights

Generic neuromolecular
imaging biomarker
identification pipeline for
brain-related disorders

Classification using
neuroepigenetic histone
deacetylase (HDAC)
enzyme imaging

[11C]Martinostat
radiotracer, PET/MR brain
imaging and Machine
Learning for diagnosis

Application to alcohol use
disorder

Article

Toward AI-driven neuroepigenetic imaging biomarker for alcohol use disorder: A proof-of-concept study

Tewodros Mulugeta Dagnew,[1] Chieh-En J. Tseng,[1] Chi-Hyeon Yoo,[1] Meena M. Makary,[1,6] Anna E. Goodheart,[7] Robin Striar,[1] Tyler N. Meyer,[1] Anna K. Rattray,[1] Leyi Kang,[1] Kendall A. Wolf,[1] Stephanie A. Fiedler,[1] Darcy Tocci,[1] Hannah Shapiro,[10] Scott Provost,[10] Eleanor Sultana,[10] Yan Liu,[1] Wei Ding,[5] Ping Chen,[4] Marek Kubicki,[8,9] Shiqian Shen,[3] Ciprian Catana,[1] Nicole R. Zürcher,[1] Hsiao-Ying Wey,[1] Jacob M. Hooker,[1] Roger D. Weiss,[2,10,*] and Changning Wang[1,11,*]

SUMMARY

Alcohol use disorder (AUD) is a disorder of clinical and public health significance requiring novel and improved therapeutic solutions. Both environmental and genetic factors play a significant role in its pathophysiology. However, the underlying epigenetic molecular mechanisms that link the gene-environment interaction in AUD remain largely unknown. In this proof-of-concept study, we showed, for the first time, the neuroepigenetic biomarker capability of non-invasive imaging of class I histone deacetylase (HDAC) epigenetic enzymes in the _in vivo_ brain for classifying AUD patients from healthy controls using a machine learning approach in the context of precision diagnosis. Eleven AUD patients and 16 age- and sex-matched healthy controls completed a simultaneous positron emission tomography-magnetic resonance (PET/MR) scan with the HDAC-binding radiotracer [^{11}C]Martinostat. Our results showed lower HDAC expression in the anterior cingulate region in AUD. Furthermore, by applying a genetic algorithm feature selection, we identified five particular brain regions whose combined [^{11}C]Martinostat relative standard uptake value (SUVR) features could reliably classify AUD vs. controls. We validate their promising classification reliability using a support vector machine classifier. These findings inform the potential of _in vivo_ HDAC imaging biomarkers coupled with machine learning tools in the objective diagnosis and molecular translation of AUD that could complement the current diagnostic and statistical manual of mental disorders (DSM)-based intervention to propel precision medicine forward.

INTRODUCTION

Alcohol use disorder (AUD) is associated with significant adverse health-related outcomes for affected individuals, as well as deleterious effects on society and the economy. The Diagnostic & Statistical Manual of Mental Disorders, 5th edition (DSM-5) defines AUD along a continuum of mild to severe disorders, according to endorsement of 11 possible symptoms, including inability to stop or control drinking and multiple related adverse sequelae. In 2020, 10.2% of the United States population (28.3 million people) aged 12 years and over had a past-year AUD and only an estimated 7% of people with AUD receive any treatment in a given year, resulting in high morbidity and mortality.[1] In addition, both the cost of treatment and economic loss totals nearly $250 billion per year.[2] AUD is often accompanied by comorbidity with other mental illnesses, negative physical health outcomes, cravings, high relapse rates, and increased social and occupational problems.[3–10] While overcoming AUD is a complex process requiring significant personal commitment, treatments including behavioral treatments, mutual support groups, and medication therapies are available.[11] Cognitive and behavioral treatment, with or without pharmaceutical interventions,

[1]Athinoula A. Martinos Center for Biomedical Imaging, Department of Radiology, Massachusetts General Hospital, Harvard Medical School, Boston, MA, USA
[2]Department of Psychiatry, Harvard Medical School, Boston, MA, USA
[3]Department of Anesthesia, Critical Care and Pain Medicine, Massachusetts General Hospital, Harvard Medical School, Boston, MA, USA
[4]Department of Engineering, University of Massachusetts Boston, Boston, MA, USA
[5]Department of Computer Science, University of Massachusetts Boston, Boston, MA, USA
[6]Systems and Biomedical Engineering Department, Cairo University, Giza, Egypt
[7]Department of Neurology, Massachusetts General Hospital, Boston, MA, USA
[8]Department of Psychiatry, Massachusetts General Hospital, Harvard Medical School, Boston, MA, USA
[9]Psychiatry Neuroimaging Laboratory, Departments of Psychiatry and Radiology, Brigham and Women's Hospital, Harvard Medical School, Boston, MA, USA
[10]Division of Alcohol, Drugs, and Addiction, McLean Hospital, Belmont, MA, USA
[11]Lead contact
*Correspondence: rweiss@mclean.harvard.edu (R.D.W.), cwang15@mgh.harvard.edu (C.W.)
https://doi.org/10.1016/j.isci.2024.110159

remain the most commonly used methods; however, their efficacy is limited.[12] There remains a need for a further understanding of the underlying pathophysiology and neurocircuitry changes necessary for successful therapy.

In the development of AUD, both genetic and environmental factors play important roles which are linked through epigenetic mechanisms. Supporting this, findings on epigenetics have revealed that AUD may have a strong connection with dysfunction of chromatin-modifying epigenetic enzymes that are frequently implicated.[13–19] Recent evidence suggests new promising therapeutic approaches for brain disorders that target enzymes involved in neuroepigenetic mechanisms.

Among these epigenetic mechanisms, alteration of histone acetylation by histone deacetylases (HDACs) has been extensively investigated in diverse disciplines, hypothesizing that the dysfunction of HDACs may lead or contribute to brain disease[20–24] including AUD.[3,25] HDACs are a family of epigenetic enzymes that regulate gene expression in the human brain by chemically modifying chromatin, the fundamental network of proteins and DNA in chromosomal structure. HDACs drive chromatin changes in response to life experience and the environment, creating a dynamic feedback system between genes and the environment. Inhibition of histone acetylation by HDACs has been implicated in reduction of alcohol consumption and relapse, lower motivation to self-administer alcohol, and reduction of alcohol withdrawal symptoms in rodent models.[3,25] These rodent studies have demonstrated that the treatment with ethanol could upregulate the histone acetylation levels in several brain regions, such as the prefrontal cortex. In addition, several HDAC isoforms, such as HDAC2 and HDAC3, are reported to increase as the treatment of ethanol in human neuronal cell line or in the amygdala. The treatment of these HDAC inhibitors could reverse ethanol-induced tolerance, anxiety, and ethanol drinking with upregulated histone acetylation level in the amygdala of rats. The treatment could reduce ethanol-induced behaviors and diminish the motivation to consume ethanol as well.

Until recently, the density and distribution of HDACs in the brain could not be quantified without sampling tissue, which is an obvious barrier when studying living humans.[20] Measuring and quantifying HDAC enzyme expression density *in vivo* is an important step toward diagnostic and therapeutic breakthroughs in CNS and neuropsychiatric disease intervention.[20,21,26] This can be done with PET and the [11C]Martinostat radiotracer, which targets class I HDAC enzymes.[26]

In this paper, we discuss our methods and findings regarding the first *in vivo* neuro-epigenetic biomarker discovery in patients with AUD in the context of precision diagnosis. We conducted a proof-of-concept positron emission tomography-magnetic resonance (PET/MR) imaging brain study with [11C]Martinostat radiotracer on AUD patients and healthy control subjects. With simultaneous PET/MR imaging, we can acquire *in vivo* imaging of the brain non-invasively. We first compared *in vivo* regional HDAC expression across the whole brain in AUD patients and healthy control subjects. We then aimed to extend the utility of *in vivo* regional HDAC expression density to help detect AUD by applying machine learning techniques. As artificial intelligence (AI) is becoming ubiquitous, machine learning based classification of PET imaging is gaining attention and holds promise of future diagnosis, prognosis and biomarker identification in the context of several diseases.[27–41] Our motivation for this work stems from analyzing patterns of subtle regional brain HDAC differences between AUD and controls that aid *in vivo-in silico* classification (i.e., imaging based diagnostic biomarker). In order to achieve this goal, regional HDAC expression densities were used as feature vectors (that characterize the subjects) for a machine learning pattern recognition model to classify patients with AUD and healthy controls.

Briefly, our methodology followed the following approach: by applying a feature selection method (i.e., genetic algorithm), we identify relevant five brain regions whose [11C]Martinostat uptake values have the potential to be a biomarker for PET/MR neuro-epigenetics based detection/diagnosis of AUD patients. We validated the differentiation capacity of the identified imaging biomarkers on whether the subject is either an AUD patient or a healthy control subject, using support vector machine (SVM) classification method and reported a satisfactory classification results that signify the promising detection/diagnostic reliability of the identified imaging biomarkers. The proposed imaging pipeline and computer aided detection system for AUD patients using [11C]Martinostat PET/MR imaging and AI has the potential to be used generically in the context of precision diagnosis for other brain related disorders too, especially in neuroepigenetic imaging based brain disorder detection/diagnosis and furthermore augments the Diagnostic and Statistical Manual of Mental Disorders (DSM) criteria based interventions that is in line with the motives of the National Institute of Mental Health's (NIMH) research domain criteria (RDoC) that encourages multi perspective view of brain related disorders to advance our holistic understanding of the etiology.

RESULTS

Lower HDAC enzyme expression in AUD patients in the anterior cingulate region

The whole brain voxel-wise comparison of the HDAC expression density image estimated as standardized uptake value ratio with a whole brain reference region ($SUVR_{WB}$) between groups shows participants with AUD exhibited a lower [11C]Martinostat uptake in the anterior cingulate area compared to healthy controls (CNT) ($Z > 2.3$, $p_{cluster} < 0.05$) (Figure 1). Table 1 shows the MNI coordinate and the Z score of the region with lower [11C]Martinostat uptake. Region of interest (ROI) wise analysis using ROIs based on FreeSurfer's Desikan-Killiany brain atlas showed no significant difference in [11C]Martinostat uptake (Figure S1). The difference in these results may be because the whole brain voxel-wise analysis is not constrained by anatomical landmarks and the cluster where group differences were found crossed the borders between cingulate and neighboring regions and also accounts to the limited spatial resolution of PET.

HDAC enzyme expression (SUVR feature) from single brain region for classification of AUD vs. control

With the aim of identifying single brain regions with the potential to differentiate AUD patients from controls according to differences in HDAC enzyme density expression, we applied SVM machine learning classification using $SUVR_{WB}$ feature from each ROI separately. We tested linear and radial basis function (RBF) kernels and found that SVM with RBF kernel performs better in classifying. V_35 (*left-caudal middle*
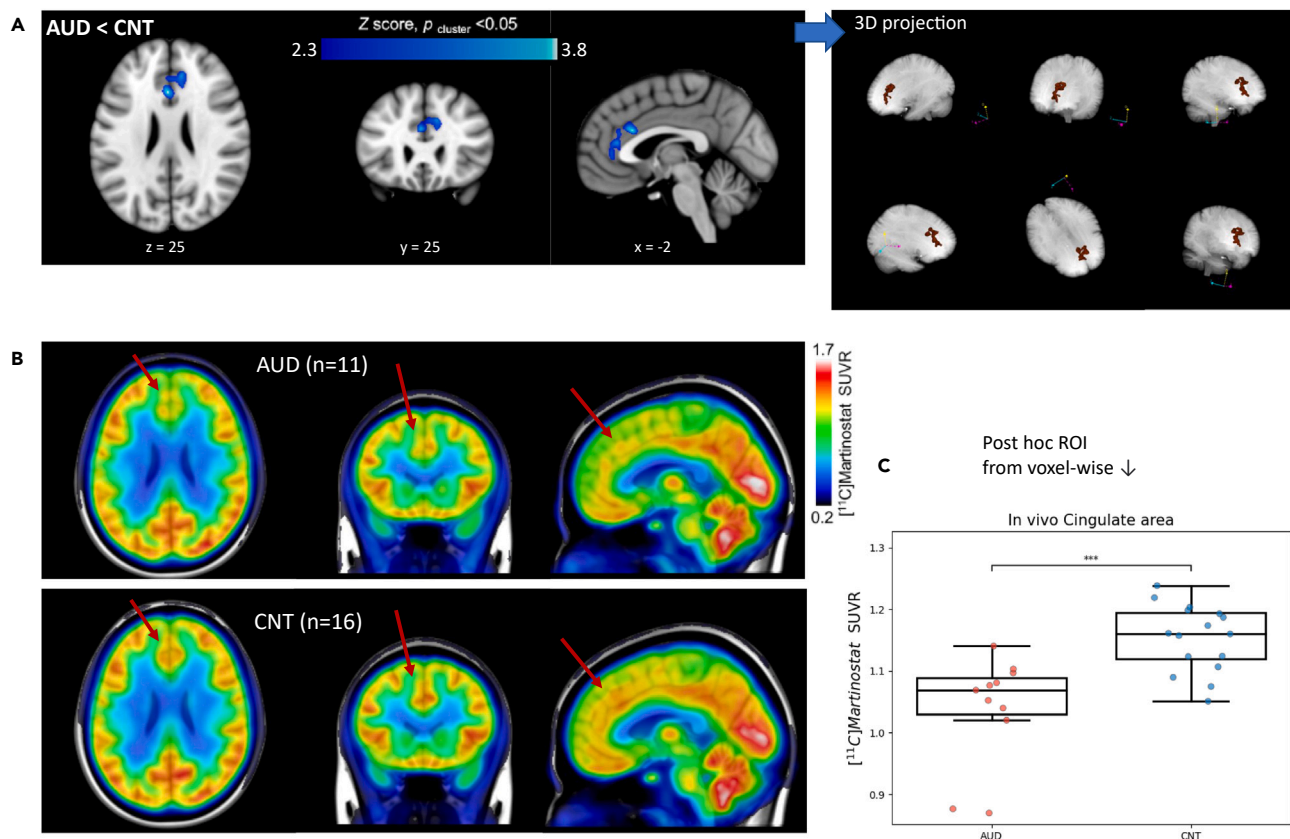
Figure 1. Whole brain voxel-wise group difference

(A) [^{11}C]Martinostat uptake is lower in the *anterior cingulate cortex* in participants with alcohol use disorder (AUD) compared to age-sex matched healthy controls (CNT). Statistical maps from voxel-wise comparison of SUVR$_{WB}$ images between matched groups, overlaid onto the MNI 1 mm template in radiological orientation ($Z > 2.3$, pcluster < 0.05). Blue-light blue represents regions significantly lower in AUD ($n = 11$) compared to CNT ($n = 16$). 3D projection of the voxel-wise group difference cluster. Anterior Cingulate and nearby areas where the HDAC expression density is lower in AUD patients compared to CNT.

(B) Group mean SUVR$_{WB}$ images. The red color indicates a higher and the blue color indicates a lower HDAC enzyme presence.

(C) Boxplot of SUVR$_{WB}$ feature values show statistically significant differences for the post hoc ROIs (mostly covering the anterior cingulate area) from the voxel-wise analysis result.

frontal cortex), V_61 (*left-superior temporal cortex*), V_51(*left-parstriangularis cortex*) and V_77 (*right-lateral orbitofrontal cortex*) stood out with relatively better classification performance (with higher F1 score) indicating their biomarker potential in detecting or classifying AUD. Furthermore, we assessed if using different tissue reference regions to generate SUVR would result in more accurate classification. We tested whole brain tissue and pons as a reference region to estimate the SUVR$_{WB}$ and SUVR$_{pons}$ for the 100 brain ROIs, and we found that SUVR$_{WB}$ resulted in better classification performance in most of the ROIs as shown with radar plot and bar chart in Figures 2A and 2B. See Figure S2–S10 for all the other classification metrics of the 100 brain ROIs using SUVR feature with SVM.

Table 1. Whole brain voxel-wise analysis reveals [^{11}C]Martinostat SUVR$_{wb}$ differences between AUD patients and healthy controls (CNT)

MNI coordinate (mm)	Z score	Anatomical region
x = −2, y = 22, z = 25	3.83	Anterior Cingulate
x = −4, y = 34, z = 13	3.47	Anterior Cingulate
x = 10, y = 35, z = 24	3.45	Anterior Cingulate
x = 2, y = 40, z = 6	3.41	Anterior Cingulate
x = 11, y = 24, z = 33	3.3	Cingulate Gyrus
x = 1, y = 33, z = 23	3.06	Anterior Cingulate

An unpaired t test with cluster thresholding ($Z > 2.3$ and P$_{cluster}$ < 0.05) was performed using SUVR$_{WB}$ images from $n = 11$ subjects with AUD and $n = 16$ controls. MNI coordinates, Z statistics, and anatomical regions are listed for areas significantly lower (AUD < CNT) in subjects with AUD compared with controls. Voxel-wise analysis AUD < CNT, cluster size: 2,921 voxels, P$_{cluster}$ < 0.05.
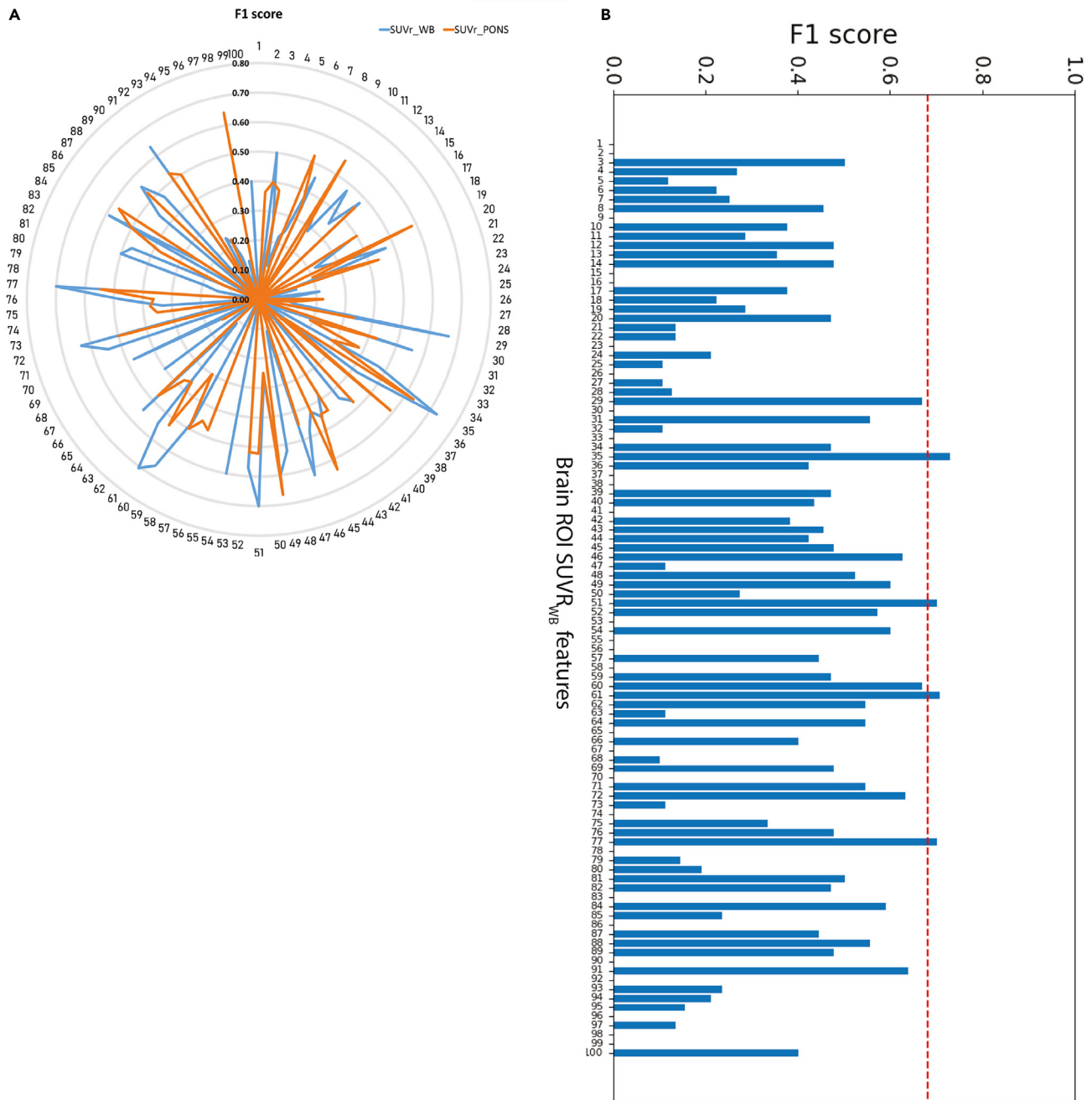
Figure 2. Classification evaluation of each single ROI's HDAC enzyme distribution density

(A) Radar plot and (B) bar chart showing the F1 score classification of individual brain ROIs SUVR feature in differentiating AUD vs. CNT using SVM machine learning classification algorithm. In the radar plot, the blue curve indicates the F1 score of the [^{11}C]Martinostat SUVR$_{WB}$ feature of the 100 brain regions, whereas the orange curve shows the F1 score metric of the [^{11}C]Martinostat SUVR$_{PONS}$ features. The following regions' SUVR$_{WB}$ features demonstrate a relatively higher F1 score in the classification process: V_35 (left-caudal middle frontal cortex) = 73%, V_61 (left-superior temporal cortex) = 71%, V_51 (left-parstriangularis cortex) = 70%, and V_77 (right-lateral orbitofrontal cortex) = 70%.

Next, we assessed the possibility of achieving a higher classification performance using a combination of SUVR$_{WB}$ features from multiple ROIs. We implemented a heuristic-based relevant feature selection method, "genetic algorithm," to identify the optimal relevant brain regions that differentiated AUD patients from matched controls according to SUVR$_{WB}$ neuro-epigenetic features. Lastly, the identified optimal brain regions were considered as a PET imaging-based diagnostic neuro-epigenetic biomarker.

Identified SUVR biomarker brain regions using genetic algorithm feature selection for classification of AUD vs. control

Using genetic algorithm, selected features evolved to have better fitness (i.e., classification accuracy) across generations (Figure 3A). In the 100th generation, the selected features achieved, on average, 90% accuracy. Figure 3B shows which features were frequently selected across the 100 trials. We repeated 100 trials because the genetic algorithm is a pseudo-random algorithm, where each run results in slightly different results due to the variability in the random generation of the initial population. The anatomical regions of the five most frequently selected relevant brain ROIs based on their $SUVR_{WB}$ value that have the potential to be biomarkers for PET/MR neuro-epigenetics-based detection of AUD patients are shown in Figure 3C. The selected relevant brain ROIs are the left hemisphere cuneus cortex, the left hemisphere superior temporal cortex, the left hemisphere temporal pole, the right hemisphere accumbens area and right hemisphere posterior cingulate (Table 2).

Neuroepigenetic imaging biomarker validation using machine learning classification

The classification power of the identified biomarkers is validated with SVM classification using a leave-one-out cross-validation approach. As shown in the confusion matrix (Table 3), only 4 out of 27 subjects are misclassified. Among them, 3 AUD patients are misclassified as controls, and 1 control subject is misclassified as an AUD patient.

As presented in Table 4, the $SUVR_{WB}$ features from the brain ROIs selected by the genetic algorithm as relevant features achieved the highest classification performance with SVM classifier; *85% accuracy, 80% f1-score, 0.83 AUC, 73% sensitivity, 93.8% specificity, 89% positive predictive value, 83.3 negative predictive value, 0.7 Matthews correlation coefficient, and 0.7 Cohen's kappa coefficient.* These results indicate that the HDAC density quantified by the [11C]Martinostat uptake in these brain regions can be a potential PET/MR based neuro-epigenetic classification biomarkers for AUD diagnosis.

When we assessed these brain regions individually (Table 4), the left superior temporal cortex $SUVR_{WB}$ feature alone achieved a noteworthy result: *81.5% accuracy, 70.6% f1-score, 0.77 AUC, 54% sensitivity, 100% specificity, 100% positive predictive value, 76.2 negative predictive value, 0.64 Matthews correlation coefficient, and 0.59 Cohen's kappa coefficient.* This result indicates that class I HDAC expression density in the left superior temporal cortex varies significantly between AUD patients and matched controls and may classify or diagnose AUD patients more accurately than other brain regions.

The discrimination capacity of the identified neuro-epigenetic biomarkers in the identified 5 regions of the brain is compared with all brain $SUVR_{WB}$ features concatenated without feature selection and a random classifier. As depicted in Figure 4, the identified neuro-epigenetic biomarkers achieved 0.83 AUC. In comparison, when using all the 100 brain regions the result was only 0.56 AUC. All the AUC results are reported in Table 4.

Correlations of HDAC enzyme expression density (SUVR) within the identified biomarker regions in AUD vs. CNT

In an exploratory fashion, we also assessed how the $SUVR_{WB}$ features in the identified biomarker regions are correlated with each other and also reported the distribution of the features (used to train the ML model) among each class (i.e., AUD vs. CNT) in Figures 5A and 5B; and Table 5.

Within the identified biomarker ROIs, for all the pairs within the AUD group, there is a positive correlation on HDAC-I expression except between left cuneus and right posterior cingulate which exhibited a negative correlation. In the CNT group, positive correlation is exhibited only between (1) the left superior temporal and left temporal pole, (2) the left superior temporal and right posterior cingulate, and (3) the left temporal pole and right posterior cingulate. There was negative correlation only between (1) the left cuneus and left superior temporal, (2) the left cuneus and left temporal pole, (3 the left cuneus and right posterior cingulate, and (4) the right accumbens and the left superior temporal. There was almost no correlation between (1) the right accumbens and the left cuneus, (2) the right accumbens and the left temporal pole, and (3) the right accumbens and the right posterior cingulate. In regions (1) the right accumbens and the left superior temporal, (2) the left cuneus and the left superior temporal, and (3) the left cuneus and left temporal pole, the AUD group showed a positive correlation, while the CNT group showed a negative correlation. In regions between (1) the left superior temporal and the left temporal pole, (2) left superior temporal and the right posterior cingulate, and (3) the left temporal pole and the right posterior cingulate, both groups showed positive correlation. Only in the region between the left cuneus and the right posterior cingulate, both groups showed a negative correlation, with the CNT group showing a more negative correlation.

DISCUSSION

AUD is a debilitating addiction illness with multifaceted pathology. A number of structural, functional, and molecular neuroimaging studies implicate there are varying measured biological features when compared with matched healthy controls.[42–48] However, the molecular mechanisms underpinning these observations in humans are not fully elucidated. In this study, we used [11C]Martinostat PET brain imaging to measure and compare relative HDAC expression levels in AUD and CNT for the first time, since epigenetic mechanisms, mainly those regulated by HDACs, have the potential to reconcile contributions of both genetic and environmental factors in AUD. The demography of the study participants is shown in Table 6. Furthermore, we presented a machine learning approach for identifying *in vivo* HDAC biomarkers for non-invasive imaging-based precision detection and classification and we identified relevant brain regions to consider potential imaging biomarkers. To this date, in this relatively new area of investigation, there are only 5 human HDAC PET brain imaging studies.[21–24,26]

Our first result on the group difference voxel-wise analysis indicated lower relative HDAC expression in the anterior cingulate and very nearby areas of AUD patients. The cingulate region is involved in various functions, including emotional processing, cognitive control,
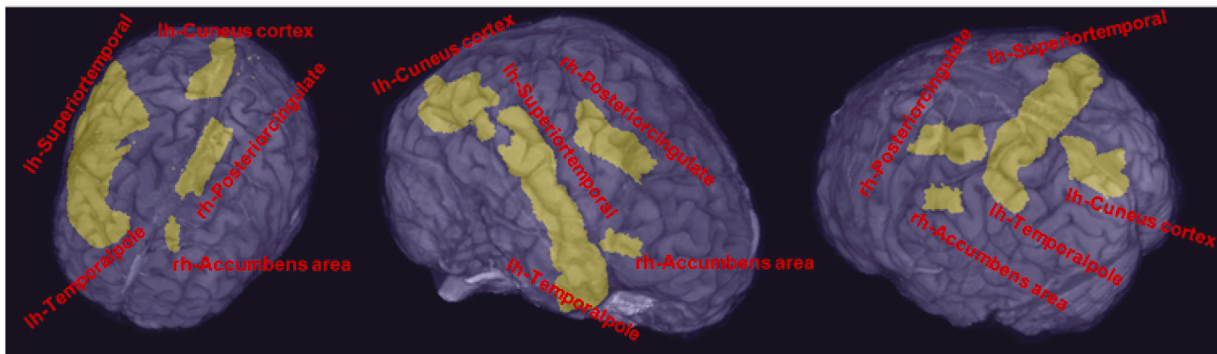
A
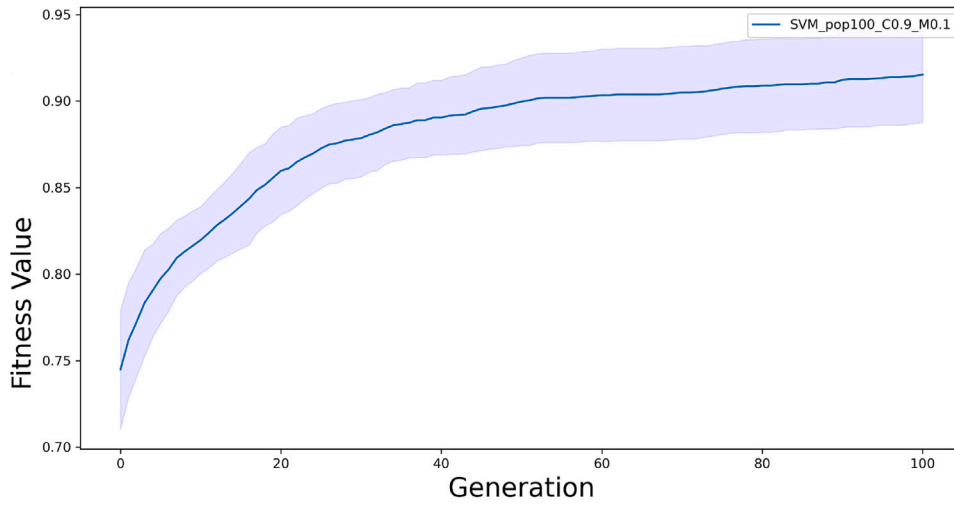
B
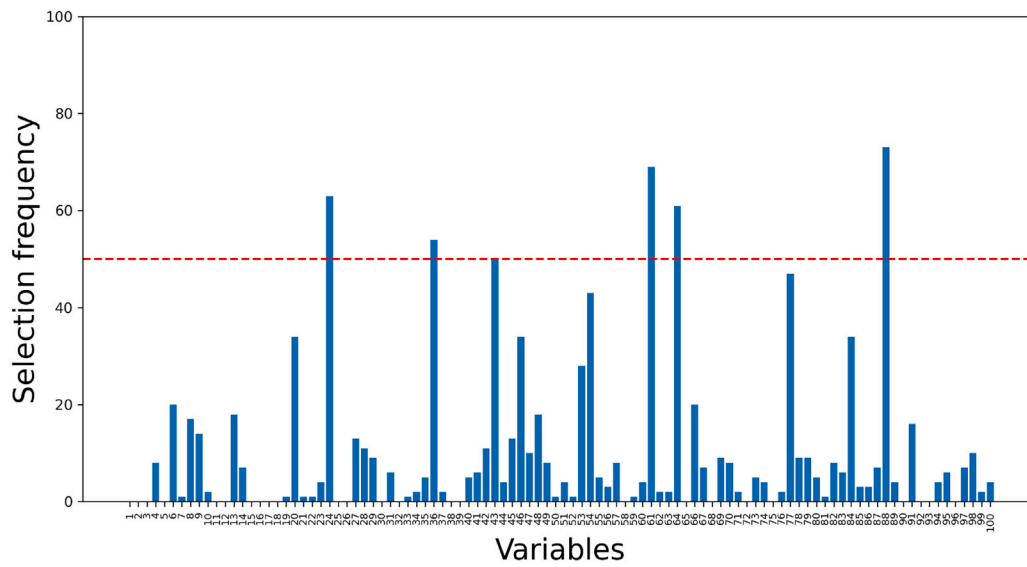
C

Figure 3. Feature selection result

(A) Genetic algorithm evolution curve. Fitness value (SVM accuracy) evolution across 100 generations.

(B) Feature selection result using model based genetic algorithm with SVM. *Right hemisphere accumbens area (V_24), left hemisphere cuneus cortex (V_36), left hemisphere superior temporal cortex (V_61), left hemisphere temporal pole cortex (V_64), right hemisphere posterior cingulate (V_88)* are selected more than 50% of the time across the 100 selection trials.

(C) 3D illustrations of the Identified biomarker $SUVR_{WB}$ brain regions for PET/MR neuro-epigenetics based classification of AUD patients.

attention regulation, behavior, motivation, and memory that are clearly affected and dysregulated in AUD patients. [11C]Martinostat PET imaging is an effective way of visualizing and quantifying class-I HDAC enzyme density and distribution non-invasively in the *in vivo* human brain. As a preliminary PET brain image feature (i.e., regional $SUVR_{wb}$) assessment, we checked if there are significant group differences in a single ROI level (where the region boundaries are estimated using FreeSurfer's Desikan-Killiany brain atlas) using a statistical test. The lack of significant differences in single regional uptake of [11C]Martinostat (i.e., HDAC enzyme expression density) was actually one of the driving forces of this work to look into non-trivial way for recognizing AUD's underlying molecular pathological features by implementing advanced feature selection algorithm approach to identify subtle combined feature patterns and be able to differentiate AUD vs. CNT. Considering the relatively small sample size of this study and large numbers of ROIs (mostly with small areas) tested with multiple comparison correction, it is possible that the detection power in single regional statistical comparison might not meet the significance level. Here it is also important to take into consideration the neurobiology of HDAC enzyme activities that due to the pleiotropic effects of HDACs on gene transcription, small changes in HDAC expression could have a large impact on neural circuits.[26] Comparing the single ROI-wise analysis with the whole brain voxel-wise group difference analysis, it is important to note that whole brain voxel-wise analysis is not constrained by anatomical landmarks and the cluster where group differences were found, slightly crossed borders between the anterior cingulate and neighboring regions. In the ROI analysis, the $SUVR_{wb}$ image voxel values found in a boundary-defined region are averaged and compared.

To make our approach clinically applicable as a precision medicine tool especially for detection and diagnosis, we leveraged machine learning/AI concepts to identify and validate multi-regional HDAC imaging biomarker. The approach could also be useful for the case of testing new therapeutics and monitoring the HDAC changes-based diagnosis. Our methodology briefly followed the following approach: by applying a genetic algorithm for feature selection (Figure 6), we identify five brain region's $SUVR_{WB}$ features that have the potential to be a biomarker for PET/MR neuroepigenetics-based detection/diagnosis of AUD patients. These regions are found to be mainly in the temporal, accumbens, and cingulate parts of the brain. We validated their differentiation capacity on whether the subject is either an AUD patient or healthy control subject, using SVM classification, and reported a satisfactory classification result that signifies the promising detection/diagnostic reliability of the proposed approach. The analogous terminologies in our methodological framework concept that can be used interchangably is described in Table 7 and the machine learning based classification evaluation approach used to validate the reliability of the identified biomarkers is shown in Table 8. In the relevant biomarker regions identified by genetic algorithm feature selection, the [11C] Martinostat radiotracer uptake is slightly higher in the AUD group when compared with CNT (see Table 2). This result shows the sensitivity of ML algorithms in the differentiation of AUD vs. CNT using subtle feature difference patterns. This highlights the potential of ML algorithms in the context of PET/MR neuroepigenetic imaging-based precise detection of AUD that can further supplement clinician-derived, DSM-based diagnostic judgements. This result also demonstrates therapeutic promise for the development of HDAC inhibitors to target the identified brain regions in the context of AUD.

The proposed imaging pipeline in the form of computer-aided detection system for AUD patients using [11C]Martinostat PET/MR imaging and ML has the potential to be used generically in the context of precision diagnosis for brain related disorders, specifically in neuroepigenetic-based brain disorder detection and diagnosis scenario and furthermore has the potential to be clinically applicable as complement to DSM criteria based interventions that is in line with the motives of NIMH's research domain criteria (RDoC) that encourages multi perspective view of brain related disorders.

Furthermore, an interesting observation is that the voxel-wise group comparison showed lower HDAC expression in the anterior cingulate of AUD patients compared to CNT, on the other hand, the HDAC level was higher on AUD participants in the relevant five brain regions

Table 2. Mean [11C]Martinostat $SUVR_{WB}$ in AUD and CNT group in the relevant brain ROIs identified by genetic algorithm feature selection

| Brain ROI | $SUVR_{WB}$ | | | | |
| | AUD group | | CNT group | | |
	Mean	SD	Mean	SD
Right-accumbens-area	1.53	0.15	1.45	0.14
Left-cuneus cortex	2.16	0.19	2.08	0.16
Left-superior temporal cortex	1.45	0.09	1.38	0.06
Left-temporal pole cortex	0.96	0.13	0.90	0.11
Right-posterior cingulate cortex	1.68	0.10	1.62	0.07

Mean and standard deviation of relative [11C]Martinostat uptake values (i.e., $SUVR_{WB}$) in the selected brain regions (i.e., identified neuroepigenetics HDAC biomarker regions) in AUD and control groups. The AUD group shows a slightly higher mean $SUVR_{WB}$ (i.e., a higher HDAC enzyme expression density) value.

Table 3. Confusion matrix of SUVR$_{wb}$ classification result of the identified neuroepigenetic biomarkers for diagnosis of AUD using SVM classifier

		True incidence/Clinical diagnosis	
		AUD	Control
ML Classification	AUD	8	1
	Control	3	15

True positive (TP) = 8, false positive (FP) = 1, true negative (TN) = 15, false negative (FN) = 3.

identified by the feature selection algorithm suggesting and reinforcing other research results on AUD that HDAC inhibitors might play a vital role in AUD therapeutic treatment.

Briefly, our study presents two major findings. First, we provide *in vivo* evidence that HDAC expression in the anterior cingulate region is decreased in participants with AUD compared to matched control subjects. Second, aligning with goals of precision medicine, this study demonstrates the potential utility of [11C]Martinostat PET/MR imaging as a biomarker and machine learning-based approaches for individualized detection and classification of AUD patients that also has the potential to be used in the case of new drug testing that targets HDACs. We identified five relevant brain regions whose combined SUVR$_{WB}$ values have the potential to serve as objective imaging-based biomarker. By applying a genetic algorithm feature selection, we identified the following five relevant particular brain regions—the left hemisphere (lh)-cuneus, lh-superior temporal, lh-temporal pole, right hemisphere (rh)-accumbens area, and rh-posterior cingulate regions whose relative [11C]Martinostat standard uptake value (SUVR) features could reliably classify AUD vs. CNT. We validated those identified quantitative imaging-based biomarkers, using a SVM classifier, which achieved a promising classification performance (Table 4). Furthermore, the population-wise observation on the correlation among the SUVR features within the identified marker regions akin to a group difference investigation based on intra-population correlation (Table 5; Figure 5) suggests promising insights for delving deeper into the investigation of HDAC enzyme changes monitoring and neuroepigenetic molecular connectivity by analyzing the correlation of the [11C] Martinostat radiotracer uptake in the selected brain sub-regions over time. The coefficients derived from the correlation analyses provide insights into the strength and direction of the relationship between HDAC expression densities in the paired regions. Interpreting these results within the context of the biological function and connectivity of the brain regions might reveal intriguing patterns. For example, the negative correlation observed in CNTs but the positive correlation in AUD group between right-accumbens and left-superior temporal regions, and the same pattern between left-cuneus and left-superior temporal regions, may suggest the correlation of increasing/decreasing trends of HDAC enzymes in given region pairs might characterize some aspects of the neuromolecular pathology of brain-related disorders such as AUD and might open potential avenues for new perspective epigenetic mechanisms and pathways discovery and give insight for the necessity of longitudinal studies which is beyond the scope of this work. A study with more population on this

Table 4. SVM classification result (AUD vs. CNT) using the SUVR$_{wb}$ features from identified biomarker brain regions compared with brain regions SUVR without feature selection

SUVR$_{wb}$ features	Accuracy in %	F1- score in %	AUC	Sensitivity in %	Specificity in %	PPV in %	NPV in %	MCC	CK
All 100 ROIs (without feature selection)	59	42	0.56	36	75	50	63	0.12	0.11
Genetic algorithm feature selection results: (lh-cuneus, lh-superior temporal, lh-temporal pole, rh-accumbens area, rh-posterior cingulate)	**85**	**80**	**0.83**	**73**	93.8	89	**83.3**	**0.7**	**0.7**
lh-cuneus (V_36)	59.3	42.1	0.56	36.4	75	50	63.2	0.12	0.12
lh-superior temporal (V_61)	81.5	70.6	0.77	54.5	**100**	**100**	76.2	0.64	0.59
lh-temporal pole (V_64)	63	54.5	0.62	54.5	68.8	54.5	68.8	0.23	0.23
rh-accumbens-area (V_24)	44.4	21	0.40	18.2	62.5	25	52.6	−0.21	−0.2
rh-posterior cingulate (V_88)	70.4	55.6	0.66	45.5	87.5	71.4	70	0.37	0.35

The identified biomarker brain regions achieved a higher classification performance in distinguishing AUD patients from control groups. Bold indicates highest performance evaluation values.
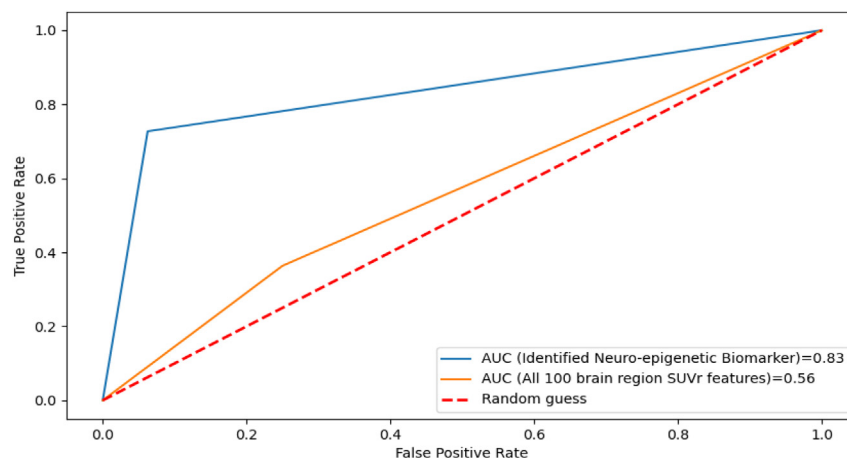
Figure 4. ROC curve of SVM classification using the identified five brain regional SUVR$_{WB}$ features

direction should shed light on undiscovered mechanisms underlying HDAC molecular connectivity pathways and the role of sub-region change patterns.

The findings from this proof-of-concept study suggest a link between altered HDAC dysfunction and AUD, indicating that pharmacological agents such as HDAC inhibitors may present a potential novel treatment for AUD. Furthermore, showing the potential of the [^{11}C]Martinostat PET imaging biomarkers coupled with machine learning tools in the objective diagnosis of AUD that could complement the current DSM based intervention to propel precision medicine forward. Further research is needed to address questions about neuroepigenetic molecular connectivity and the role of other chromatin modifying enzymes in the AUD brain and their relationship with other substance use disorders including treatment intervention studies.

Limitations of the study

We acknowledge one minor and one major limitation of this work. The minor limitation is that our study measures differences in [^{11}C]Martinostat uptake normalized to the whole-brain mean (SUVR$_{WB}$), but not absolute uptake values. Therefore, future [^{11}C]Martinostat PET studies with arterial blood sampling, which enables quantification, in larger sample sizes will reinforce our findings and the HDAC expression differences in AUD. Furthermore, it will facilitate our approach to be clinically implemented. However, authors of previous studies[21,26] clearly demonstrated that standard uptake value (SUV) normalized to whole brain mean (standard uptake value ratio, SUVR$_{WB}$) from 60 to 90 min post radiotracer injection is an appropriate surrogate measure for the HDAC distribution volume (V$_T$) in a subset of healthy young and old adults. Regional brain SUVR were strongly correlated with V$_T$ values derived from a two-tissue compartmental model (2TCM), using metabolite-corrected arterial plasma as an input function.

The major limitation of this study is the sample size and the AUD severity categories. Our work here represents a pioneering initial study that contributes to understanding the neurochemical connectome of the brain in AUD condition. The process of collecting data from 11 chronic patients with AUD spanned approximately 5 years. However, recruiting mild and moderate patients is challenging as they typically do not seek enrollment in rehabilitation centers. Furthermore, collecting data from AUD individuals is a complex and time-consuming process, as finding cooperating patients without comorbidities is extremely challenging. However, it is essential to take the initial step and build upon it as more data becomes available. Our study primarily focuses on chronic patients as they are the ones enrolled in the rehabilitation center at Mclean Hospital affiliated with Harvard Medical School. Our intention was to generate substantial knowledge within these cohorts before expanding the study to include mild and moderate patients. We approach this step by step, which is why our current work is a 'proof-of-concept' study. Hence, our investigation begins with an examination of the HDAC specific neuroepigenetic aspects of AUD patients and this work will be extended to include differential diagnosis and sub-phenotyping that will be conducted incrementally. Furthermore, we have plans of conducting investigation on the rest of 17 HDAC enzymes in humans that have never been mapped and visualized using PET as of today. By starting with these chronic patients, we establish a strong foundation of understanding before moving toward other more granular analysis. To address this challenge of small data and usage of ML algorithms, in our proof-of-concept study, we emphasized to apply the well-established leave one out cross validation strategy making sure during a training phase, the hold out test subject never participated in the model learning to prevent overfitting and double dipping. This process mimics how clinically deployed AI systems work, i.e., the already trained AI model makes inference on a newly coming patient individually. Looking ahead, our future aims include collecting more data and incorporating deep learning techniques that seamlessly integrate feature extraction, selection, and classification. The scalability of our pipeline allows for the replacement of feature selection and classification modules with alternative state-of-the-art techniques such as convolutional neural network (CNN) and transformer models. In summary, we recognize the importance of a systematic and step-by-step approach in our study, given the complexities of AUD and data collection. In this frontier, our future efforts will focus on expanding the dataset
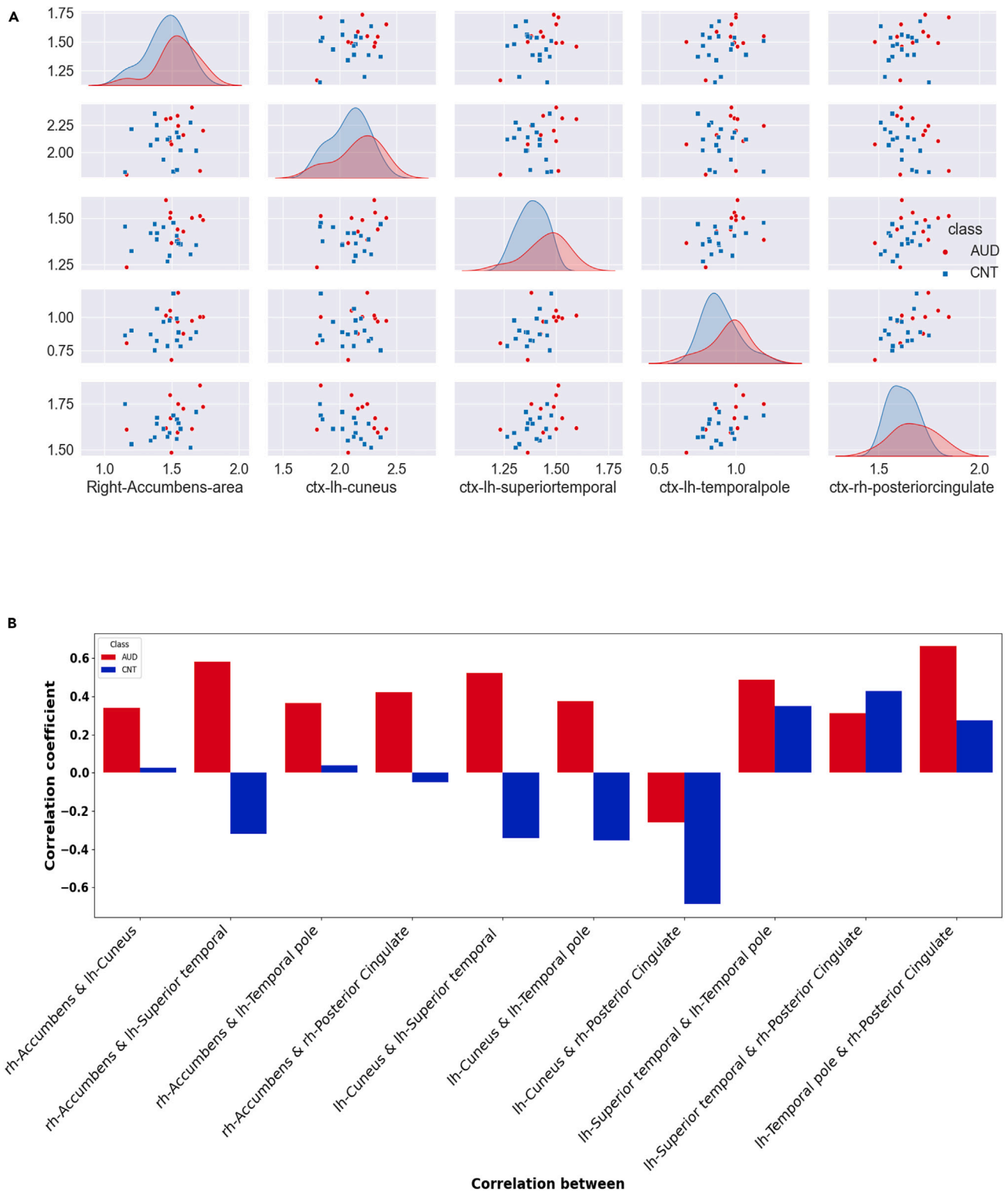
Figure 5. Statistical characteristics of the identified neuroepigenetics imaging biomarker features among AUD and CNT groups

(A) Correlogram of the identified 5 brain region SUVR$_{WB}$ values.

(B) [^{11}C]Martinostat radiotracer uptake (i.e., SUVR$_{WB}$) Pearson's correlation between the identified biomarker regions in AUD and CNT group.

Table 5. SUVR$_{wb}$ correlation among the identified biomarker regions in AUD and CNT group

Correlation b/n	In AUD	In CNT
rh-accumbens and lh-cuneus	0.34	0.03
rh-accumbens and lh-superior temporal	0.58	−0.32
rh-accumbens and lh-temporal pole	0.36	0.04
rh-accumbens and rh-posterior cingulate	0.42	−0.05
lh-cuneus and lh-superior temporal	0.52	−0.34
lh-cuneus and lh-temporal pole	0.37	−0.35
lh-cuneus and rh-posterior cingulate	−0.26	−0.69 (**p value = 0.003)
lh-superior temporal and lh-temporal pole	0.49	0.35
lh-superior temporal and rh-posterior cingulate	0.31	0.43
lh-temporal pole and rh-posterior cingulate	0.66 (* p value = 0.026)	0.28

In AUD a higher positive correlation is observed between left hemisphere (lh) temporal pole and right hemisphere (rh) posterior cingulate (*p value = 0.026). In control group a higher negative correlation is observed between left hemisphere cuneus and right hemisphere posterior cingulate (**p value = 0.003).

and leveraging deep learning to enhance our analysis pipeline. But still we showed the sensitivity of the machine learning pattern recognition in capturing the subtle HDAC difference information on few brain regions and be able to classify subjects individually and reliably. Despite these limitations, we did test potential confounding factors such as anatomical volumes, and our findings were robust to these issues. Nonetheless, a larger sample size will be needed to reinforce our findings.

STAR★METHODS

Detailed methods are provided in the online version of this paper and include the following:

- KEY RESOURCES TABLE
- RESOURCE AVAILABILITY
  - Lead contact
  - Materials availability
  - Data and code availability

Table 6. Study participant demographic information

Characteristic	AUD	Control
Number of participants	11	16
Sex (M/F)	8/3	11/5
Age range (years)	23–61	22–63
Mean age (years)	38.9 ± 14.0	38.75 ± 14.9
Race	1 B, 10 W	2 A, 3 B, 10 W, 1 M
Mean BMI	28.8 ± 5.0	26.29 ± 4.9
Injected dose (mCi)	5.27 ± 0.29	5.04 ± 0.41
Molar activity (mCi/nmol)	1.8 ± 0.73	1.9 ± 0.8

Subjects with AUD (n = 11) and healthy control subjects (n = 16) were group matched based on age and sex. Injected dose of [^{11}C]Martinostat did not differ between groups. The mean age, BMI, injected dose, and activity are represented by average ± standard deviation. A = Asian, B = Black, W = White, M = Mix.
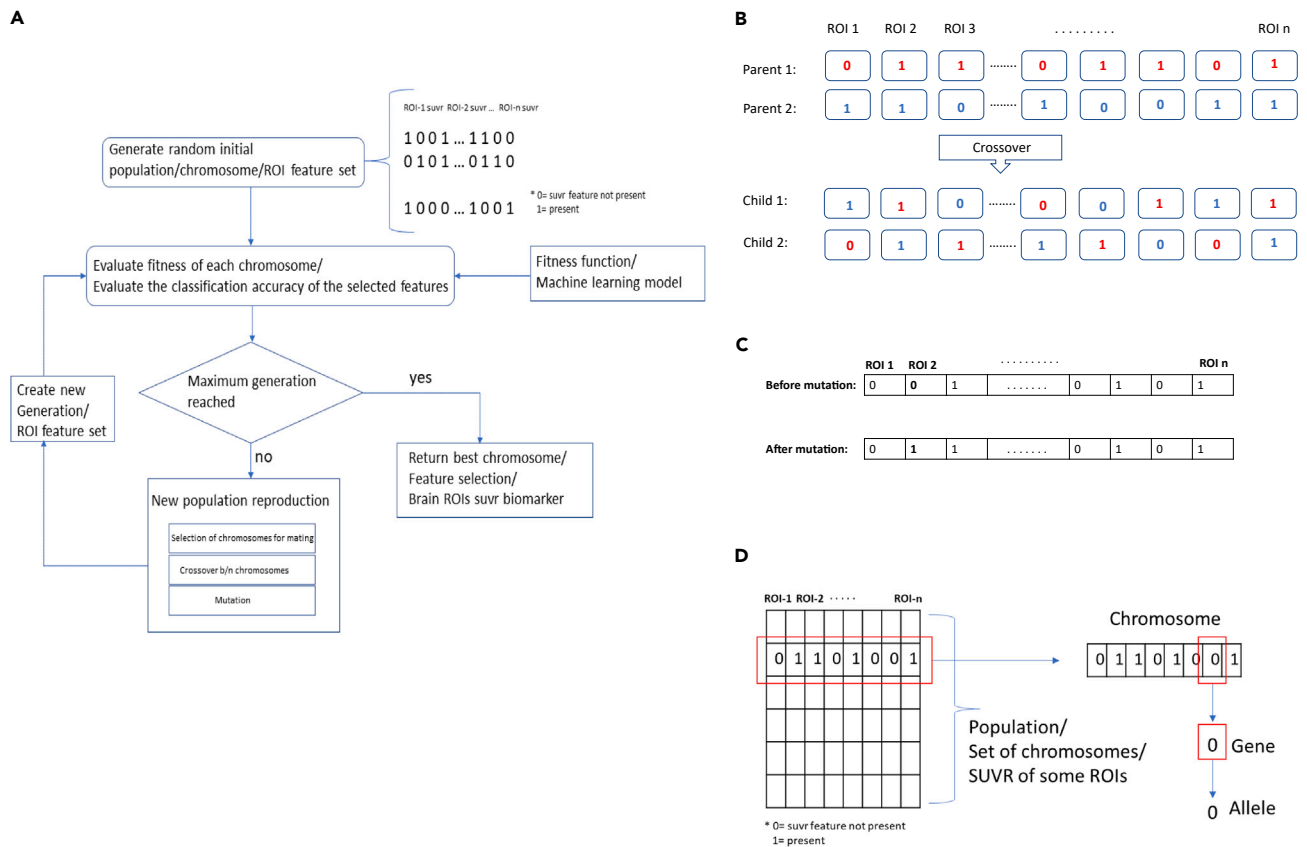
Figure 6. Model-based genetic algorithm

(A) Algorithm flow chart.

(B) An illustration of crossover. Two parent solutions exchange segments of their chromosomes. Subsequently, the fitness of each solution is assessed, and if the fitness is improved the new best solution is added to the population of solutions.

(C) An illustration of a mutation. The ROI 2 variable in the second position ("after mutation") is mutated from 0 to 1.

(D) Illustration of the genetic algorithm terminology applied to our [^{11}C]Martinostat SUVR$_{WB}$ dataset.

- EXPERIMENTAL MODEL AND STUDY PARTICIPANT DETAILS
  - Study design
  - Study participants
- METHOD DETAILS
  - Radiosynthesis of [^{11}C]Martinostat
  - PET/MRI data acquisition
  - MRI data processing and analysis
  - PET data reconstruction and analysis
  - Biomarker identification
  - Terminology equivalence

Table 7. Analogous terminologies in our methodological framework concept

Genetic algorithm terminology	Machine learning terminology	Our AUD neuroepigenetics case
Initial population	Set of feature vectors	Random combination of SUVR values/features from multiple brain regions
Chromosome	A single feature vector	Concatenated SUVR values from multiple brain region
Gene	One element of the feature vector	SUVR value from a single brain region
Fitness value	ML model classification performance	AUD vs. CNT classification reliability

Table 8. The confusion matrix provides a mechanism to assess the accuracy and overall performance of binary diagnostic classification

		True incidence/Clinical diagnosis	
		AUD	Control
ML classification	AUD	TP	FP
	Control	FN	TN

TP = true positive, FP = false positive, TN = true negative, FN = false negative.

- QUANTIFICATION AND STATISTICAL ANALYSIS
  - Machine learning classification evaluation metrics for biomarker validation

AUTHOR CONTRIBUTIONS

T.M.D. and C.W. designed and conceptualized the study. T.M.D., T.N.M., A.K.R., S.A.F., R.S., L.K., K.A.W., D.T., N.R.Z., H.Y., and C.W. contributed to collecting human imaging data and/or accompanying demographic data. T.M.D., C.-E.J.T., C.-H.Y, M.M.M., C.C., N.R.Z., H.-Y.W., and C.W. contributed to the methodology and human imaging data analysis. T.M.D., A.E.G., Y.L., S.S., N.R.Z., P.C., W.D., M.K., J.M.H., H.Y., R.D.W., S.S., and C.W. contributed to the study investigation. T.M.D. performed machine learning experiments using python. T.M.D. and C.W. wrote the original draft of the manuscript. T.M.D., C.-E.J.T., C.-H.Y., S.A.F., H.S., S.P., E.S., S.S., P.C., W.D., R.D.W. and C.W. edited the manuscript. C.W. acquired funding for the study.

DECLARATION OF INTERESTS

C.W. and J.M.H. are inventors of the [^{11}C]Martinostat epigenetic PET radiotracer imaging probe used in this project.

REFERENCES

1. Substance Abuse Mental Health Services Administration (SAMHSA) (2021). Key substance use and mental health indicators in the United States: Results from the 2020 National Survey on Drug Use and Health (HHS Publication No. PEP21-07-01-003, NSDUH Series H-56). Rockville, MD: Center for Behavioral Health Statistics and Quality (2022) (Center for Behavioral Health Statistics and Quality, Substance Abuse and Mental Health Services Administration). https://www.samhsa.gov/data.

2. Sacks, J.J., Gonzales, K.R., Bouchery, E.E., Tomedi, L.E., and Brewer, R.D. (2015). 2010 National and State Costs of Excessive Alcohol Consumption. Am. J. Prev. Med. 49, e73–e79. https://doi.org/10.1016/j.amepre.2015.05.031.

3. Jeanblanc, J., Lemoine, S., Jeanblanc, V., Alaux-Cantin, S., and Naassila, M. (2015). The Class I-Specific HDAC Inhibitor MS-275 Decreases Motivation to Consume Alcohol and Relapse in Heavy Drinking Rats. Int. J. Neuropsychopharmacol. 18, pyv029. https://doi.org/10.1093/ijnp/pyv029.

4. Green, A.I., Brunette, M.F., Dawson, R., Buckley, P., Wallace, A.E., Hafez, H., Herz, M., Narasimhan, M., Noordsy, D.L., O'Keefe, C., et al. (2015). Long-Acting Injectable vs Oral Risperidone for Schizophrenia and Co-Occurring Alcohol Use Disorder: A Randomized Trial. J. Clin. Psychiatry 76, 1359–1365. https://doi.org/10.4088/JCP.13m08838.

5. Weiss, N.H., Duke, A.A., and Sullivan, T.P. (2014). Probable Posttraumatic Stress Disorder and Women's Use of Aggression in Intimate Relationships: The Moderating Role of Alcohol Dependence. J. Trauma Stress 27, 550–557. https://doi.org/10.1002/jts.21960.

6. O'Connell, R., Chishinga, N., Kinyanda, E., Patel, V., Ayles, H., Weiss, H.A., and Seedat, S. (2013). Prevalence and Correlates of Alcohol Dependence Disorder among TB and HIV Infected Patients in Zambia. PLoS One 8, e74406. https://doi.org/10.1371/journal.pone.0074406.

7. Farren, C.K., Hill, K.P., and Weiss, R.D. (2012). Bipolar Disorder and Alcohol Use Disorder: A Review. Curr. Psychiatry Rep. 14, 659–666. https://doi.org/10.1007/s11920-012-0320-9.

8. Levy, B., Manove, E., and Weiss, R.D. (2012). Recovery of cognitive functioning in patients with co-occurring bipolar disorder and alcohol dependence during early remission from an acute mood episode. Ann. Clin. Psychiatry. 24, 143–154.

9. Levy, B., Monzani, B.A., Stephansky, M.R., and Weiss, R.D. (2008). Neurocognitive impairment in patients with co-occurring bipolar disorder and alcohol dependence upon discharge from inpatient care. Psychiatry Res. 161, 28–35. https://doi.org/10.1016/j.psychres.2007.09.009.

10. Saunders, J.B., Degenhardt, L., Reed, G.M., and Poznyak, V. (2019). Alcohol Use Disorders in ICD-11: Past, Present, and Future. Alcohol Clin. Exp. Res. 43, 1617–1631. https://doi.org/10.1111/acer.14128.

11. Witkiewitz, K., Litten, R.Z., and Leggio, L. (2019). Advances in the science and treatment of alcohol use disorder. Sci. Adv. 5, eaax4043. https://doi.org/10.1126/sciadv.aax4043.

12. Lohoff, F.W. (2022). Targeting Unmet Clinical Needs in the Treatment of Alcohol Use Disorder. Front. Psychiatry 13, 767506.

13. Wedemeyer, F., Kaminski, J.A., Zillich, L., Hall, A.S.M., Friedel, E., and Witt, S.H. (2020). Prospects of Genetics and Epigenetics of Alcohol Use Disorder. Curr. Addict. Rep. 7, 446–452. https://doi.org/10.1007/s40429-020-00331-x.

14. Chen, J., Hutchison, K.E., Bryan, A.D., Filbey, F.M., Calhoun, V.D., Claus, E.D., Lin, D., Sui, J., Du, Y., and Liu, J. (2018). Opposite Epigenetic Associations With Alcohol Use and Exercise Intervention. Front. Psychiatry 9, 594. https://doi.org/10.3389/fpsyt.2018.00594.

15. Sagarkar, S., and Sakharkar, A. (2017). Chapter 18 - Epigenetics and alcohol use disorders. In Neuropsychiatric Disorders and Epigenetics, D.H. Yasui, J. Peedicayil, and D.R. Grayson, eds. (Academic Press), pp. 361–397. https://doi.org/10.1016/B978-0-12-800226-1.00018-6.

16. Legastelois, R., Jeanblanc, J., Vilpoux, C., Bourguet, E., and Naassila, M. (2017). [Epigenetic mechanisms and alcohol use disorders: a potential therapeutic target]. Biol. Aujourdhui 211, 83–91. https://doi.org/10.1051/jbio/2017014.

17. Delcuve, G.P., Khan, D.H., and Davie, J.R. (2012). Roles of histone deacetylases in epigenetic regulation: emerging paradigms from studies with inhibitors. Clin. Epigenetics 4, 5. https://doi.org/10.1186/1868-7083-4-5.

18. Longley, M.J., Lee, J., Jung, J., and Lohoff, F.W. (2021). Epigenetics of alcohol use disorder—A review of recent advances in DNA methylation profiling. Addict. Biol. 26, e13006. https://doi.org/10.1111/adb.13006.

19. Ciafrè, S., Carito, V., Ferraguti, G., Greco, A., Chaldakov, G.N., Fiore, M., and Ceccanti, M. (2019). How alcohol drinking affects our genes: an epigenetic point of view. Biochem. Cell. Biol. 97, 345–356. https://doi.org/10.1139/bcb-2018-0248.

20. Wang, C., Schroeder, F.A., Wey, H.-Y., Borra, R., Wagner, F.F., Reis, S., Kim, S.W., Holson, E.B., Haggarty, S.J., and Hooker, J.M. (2014). In vivo imaging of histone deacetylases (HDACs) in the central nervous system and major peripheral organs. J. Med. Chem. 57, 7999–8009. https://doi.org/10.1021/jm500872p.

21. Wey, H.-Y., Gilbert, T.M., Zürcher, N.R., She, A., Bhanot, A., Taillon, B.D., Schroeder, F.A., Wang, C., Haggarty, S.J., and Hooker, J.M. (2016). Insights into neuroepigenetics through human histone deacetylase PET imaging. Sci. Transl. Med. 8, 351ra106. https://doi.org/10.1126/scitranslmed.aaf7551.

22. Tseng, C.-E.J., Gilbert, T.M., Catanese, M.C., Hightower, B.G., Peters, A.T., Parmar, A.J., Kim, M., Wang, C., Roffman, J.L., Brown, H.E., et al. (2020). In vivo human brain expression of histone deacetylases in bipolar disorder. Transl. Psychiatry 10, 224. https://doi.org/10.1038/s41398-020-00911-5.

23. Gilbert, T.M., Zürcher, N.R., Wu, C.J., Bhanot, A., Hightower, B.G., Kim, M., Albrecht, D.S., Wey, H.-Y., Schroeder, F.A., Rodriguez-Thompson, A., et al. (2019). PET neuroimaging reveals histone deacetylase dysregulation in schizophrenia. J. Clin. Invest. 129, 364–372. https://doi.org/10.1172/JCI123743.

24. Pascoal, T.A., Chamoun, M., Lax, E., Wey, H.-Y., Shin, M., Ng, K.P., Kang, M.S., Mathotaarachchi, S., Benedet, A.L.,

Therriault, J., et al. (2022). [11C]Martinostat PET analysis reveals reduced HDAC I availability in Alzheimer's disease. Nat. Commun. 13, 4171. https://doi.org/10.1038/s41467-022-30653-5.

25. Pandey, S.C., Ugale, R., Zhang, H., Tang, L., and Prakash, A. (2008). Brain Chromatin Remodeling: A Novel Mechanism of Alcoholism. J. Neurosci. 28, 3729–3737. https://doi.org/10.1523/JNEUROSCI.5731-07.2008.

26. Gilbert, T.M., Zürcher, N.R., Catanese, M.C., Tseng, C.-E.J., Di Biase, M.A., Lyall, A.E., Hightower, B.G., Parmar, A.J., Bhanot, A., Wu, C.J., et al. (2019). Neuroepigenetic signatures of age and sex in the living human brain. Nat. Commun. 10, 2945. https://doi.org/10.1038/s41467-019-11031-0.

27. Kawauchi, K., Furuya, S., Hirata, K., Katoh, C., Manabe, O., Kobayashi, K., Watanabe, S., and Shiga, T. (2020). A convolutional neural network-based system to classify patients using FDG PET/CT examinations. BMC Cancer 20, 227. https://doi.org/10.1186/s12885-020-6694-x.

28. Kim, S., Lee, P., Oh, K.T., Byun, M.S., Yi, D., Lee, J.H., Kim, Y.K., Ye, B.S., Yun, M.J., Lee, D.Y., et al. (2021). Deep learning-based amyloid PET positivity classification model in the Alzheimer's disease continuum by using 2-[18F]FDG PET. EJNMMI Res. 11, 56. https://doi.org/10.1186/s13550-021-00798-3.

29. Garraux, G., Phillips, C., Schrouff, J., Kreisler, A., Lemaire, C., Degueldre, C., Delcour, C., Hustinx, R., Luxen, A., Destée, A., and Salmon, E. (2013). Multiclass classification of FDG PET scans for the distinction between Parkinson's disease and atypical parkinsonian syndromes. Neuroimage. Clin. 2, 883–893. https://doi.org/10.1016/j.nicl.2013.06.004.

30. Xu, J., Xu, Q., Liu, S., Li, L., Li, L., Yen, T.-C., Wu, J., Wang, J., Zuo, C., Wu, P., and Zhuang, X. (2021). Computer-Aided Classification Framework of Parkinsonian Disorders Using 11C-CFT PET Imaging. Front. Aging Neurosci. 13, 792951.

31. Chang, C., Sun, X., Wang, G., Yu, H., Zhao, W., Ge, Y., Duan, S., Qian, X., Wang, R., Lei, B., et al. (2021). A Machine Learning Model Based on PET/CT Radiomics and Clinical Characteristics Predicts ALK Rearrangement Status in Lung Adenocarcinoma. Front. Oncol. 11, 603882.

32. Arabi, H., AkhavanAllaf, A., Sanaat, A., Shiri, I., and Zaidi, H. (2021). The promise of artificial intelligence and deep learning in PET and SPECT imaging. Phys. Med. 83, 122–137. https://doi.org/10.1016/j.ejmp.2021.03.008.

33. Vangu, M., Purbhoo, K., and Liu, H. (2021). Clinical Potential for Artificial Intelligence in PET Imaging: Phase 1 Result of Dose Reduction using Deep Learning Reconstruction. J. Nucl. Med. 62, 1179.

34. Seifert, R., Weber, M., Kocakavuk, E., Rischpler, C., and Kersting, D. (2021). Artificial Intelligence and Machine Learning in Nuclear Medicine: Future Perspectives. Semin. Nucl. Med. 51, 170–177. https://doi.org/10.1053/j.semnuclmed.2020.08.003.

35. Toyama, Y., Hotta, M., Motoi, F., Takanami, K., Minamimoto, R., and Takase, K. (2020). Prognostic value of FDG-PET radiomics with machine learning in pancreatic cancer. Sci. Rep. 10, 17024. https://doi.org/10.1038/s41598-020-73237-3.

36. R, S.,N.N., and J, P. (2022). Machine learning algorithms for the diagnosis of Alzheimer and Parkinson disease. J. Med. Eng. Technol. 1–9.

https://doi.org/10.1080/03091902.2022.2097326.

37. AlSaeed, D., and Omar, S.F. (2022). Brain MRI Analysis for Alzheimer's Disease Diagnosis Using CNN-Based Feature Extraction and Machine Learning. Sensors 22, 2911. https://doi.org/10.3390/s22082911.

38. Mirzaei, G., and Adeli, H. (2022). Machine learning techniques for diagnosis of alzheimer disease, mild cognitive disorder, and other types of dementia. Biomed. Signal Process Control 72, 103293. https://doi.org/10.1016/j.bspc.2021.103293.

39. Singh, N.M., Harrod, J.B., Subramanian, S., Robinson, M., Chang, K., Cetin-Karayumak, S., Dalca, A.V., Eickhoff, S., Fox, M., Franke, L., et al. (2022). How Machine Learning is Powering Neuroimaging to Improve Brain Health. Neuroinform 20, 943–964. https://doi.org/10.1007/s12021-022-09572-9.

40. Zhang, Z., and Sejdić, E. (2019). Radiological images and machine learning: Trends, perspectives, and prospects. Comput. Biol. Med. 108, 354–370. https://doi.org/10.1016/j.compbiomed.2019.02.017.

41. Ahmed, M.R., Zhang, Y., Feng, Z., Lo, B., Inan, O.T., and Liao, H. (2019). Neuroimaging and Machine Learning for Dementia Diagnosis: Recent Advancements and Future Prospects. IEEE Rev. Biomed. Eng. 12, 19–33. https://doi.org/10.1109/RBME.2018.2886237.

42. Pickens, R.W., Svikis, D.S., McGue, M., Lykken, D.T., Heston, L.L., and Clayton, P.J. (1991). Heterogeneity in the inheritance of alcoholism. A study of male and female twins. Arch. Gen. Psychiatry 48, 19–28. https://doi.org/10.1001/archpsyc.1991.01810250021002.

43. Litten, R.Z., Ryan, M.L., Falk, D.E., Reilly, M., Fertig, J.B., and Koob, G.F. (2015). Heterogeneity of alcohol use disorder: understanding mechanisms to advance personalized treatment. Alcohol Clin. Exp. Res. 39, 579–584. https://doi.org/10.1111/acer.12669.

44. Suk, J.-W., Hwang, S., and Cheong, C. (2021). Functional and Structural Alteration of Default Mode, Executive Control, and Salience Networks in Alcohol Use Disorder. Front. Psychiatry 12, 742228.

45. Crespi, C., Galandra, C., Manera, M., Basso, G., Poggi, P., and Canessa, N. (2019). Executive Impairment in Alcohol Use Disorder Reflects Structural Changes in Large-Scale Brain Networks: A Joint Independent Component Analysis on Gray-Matter and White-Matter Features. Front. Psychol. 10, 2479. https://doi.org/10.3389/fpsyg.2019.02479.

46. Fritz, M., Klawonn, A.M., and Zahr, N.M. (2022). Neuroimaging in alcohol use disorder: From mouse to man. J. Neurosci. Res. 100, 1140–1158. https://doi.org/10.1002/jnr.24423.

47. Siomek-Gorecka, A., Dlugosz, A., and Czarnecki, D. (2021). The Molecular Basis of Alcohol Use Disorder (AUD). Genetics, Epigenetics, and Nutrition in AUD: An Amazing Triangle. Int. J. Mol. Sci. 22, 4262. https://doi.org/10.3390/ijms22084262.

48. Ron, D., and Barak, S. (2016). Molecular mechanisms underlying alcohol-drinking behaviours. Nat. Rev. Neurosci. 17, 576–591. https://doi.org/10.1038/nrn.2016.85.

49. Kolb, A., Wehrl, H.F., Hofmann, M., Judenhofer, M.S., Eriksson, L., Ladebeck, R., Lichy, M.P., Byars, L., Michel, C., Schlemmer, H.-P., et al. (2012). Technical performance evaluation of a human brain PET/MRI system.

Eur. Radiol. *22*, 1776–1788. https://doi.org/10.1007/s00330-012-2415-4.

50. Tisdall, M.D., Hess, A.T., Reuter, M., Meintjes, E.M., Fischl, B., and van der Kouwe, A.J.W. (2012). Volumetric navigators for prospective motion correction and selective reacquisition in neuroanatomical MRI. Magn. Reson. Med. *68*, 389–399. https://doi.org/10.1002/mrm.23228.

51. David, I.-G., Ae, H., Stefan, F., Didier, B., Sylvia, S., Sebastian, F., Kt, C., Db, C., and Ciprian, C. (2014). An SPM8-based approach for attenuation correction combining segmentation and nonrigid template formation: application to simultaneous PET/MR brain imaging. Journal of nuclear medicine : official publication, Society of Nuclear Medicine *55*, 1825–1830. https://doi.org/10.2967/jnumed.113.136341.

52. Chonde, D.B., Izquierdo-Garcia, D., Chen, K., Bowen, S.L., and Catana, C. (2014). Masamune: a tool for automatic dynamic PET data processing, image reconstruction and integrated PET/MRI data analysis. EJNMMI Phys. *1*, A57. https://doi.org/10.1186/2197-7364-1-S1-A57.

53. Arbabshirani, M.R., Plis, S., Sui, J., and Calhoun, V.D. (2017). Single subject prediction of brain disorders in neuroimaging: Promises and pitfalls. Neuroimage *145*, 137–165. https://doi.org/10.1016/j.neuroimage.2016.02.079.

54. Smith, S.M., Jenkinson, M., Woolrich, M.W., Beckmann, C.F., Behrens, T.E.J., Johansen-Berg, H., Bannister, P.R., De Luca, M., Drobnjak, I., Flitney, D.E., et al. (2004). Advances in functional and structural MR image analysis and implementation as FSL. Neuroimage *23*, S208–S219. https://doi.org/10.1016/j.neuroimage.2004.07.051.

55. Hearst, M.A., Dumais, S.T., Osuna, E., Platt, J., and Scholkopf, B. (1998). Support vector machines. IEEE Intell. Syst. Their Appl. *13*, 18–28. https://doi.org/10.1109/5254.708428.

56. Li, Z., McIntyre, R.S., Husain, S.F., Ho, R., Tran, B.X., Nguyen, H.T., Soo, S.-C., Ho, C.S., and Chen, N. (2022). Identifying neuroimaging biomarkers of major depressive disorder from cortical hemodynamic responses using machine learning approaches. EBioMedicine *79*, 104027. https://doi.org/10.1016/j.ebiom.2022.104027.

57. Huo, Y., Jin, D., Zhang, Y., Guo, D., and Wang, Z. (2022). Editorial: Machine Learning for Quantitative Neuroimaging Analysis. Front. Neurosci. *16*, 925819. https://doi.org/10.3389/fnins.2022.925819.

58. Cho, K., Kim, W.-G., Kang, H., Yang, G.-S., Kim, H.-W., Jeong, J.-E., Yoon, H.-J., Jeong, Y.-J., and Kang, D.-Y. (2019). Classification of 18F-Florbetaben Amyloid Brain PET Image using PCA-SVM. Biomed Sci Letters *25*, 99–106. https://doi.org/10.15616/BSL.2019.25.1.99.

59. Shakarami, A., Tarrah, H., and Mahdavi-Hormat, A. (2020). A CAD system for diagnosing Alzheimer's disease using 2D slices and an improved AlexNet-SVM method. Optik *212*, 164237. https://doi.org/10.1016/j.ijleo.2020.164237.

60. Zhou, T., Thung, K.-H., Liu, M., Shi, F., Zhang, C., and Shen, D. (2020). Multi-modal latent space inducing ensemble SVM classifier for early dementia diagnosis with neuroimaging data. Med. Image Anal. *60*, 101630. https://doi.org/10.1016/j.media.2019.101630.

61. Yassin, W., Nakatani, H., Zhu, Y., Kojima, M., Owada, K., Kuwabara, H., Gonoi, W., Aoki, Y., Takao, H., Natsubori, T., et al. (2020). Machine-learning classification using neuroimaging data in schizophrenia, autism, ultra-high risk and first-episode psychosis. Transl. Psychiatry *10*, 278. https://doi.org/10.1038/s41398-020-00965-5.

62. Flint, C., Cearns, M., Opel, N., Redlich, R., Mehler, D.M.A., Emden, D., Winter, N.R., Leenings, R., Eickhoff, S.B., Kircher, T., et al. (2021). Systematic misestimation of machine learning performance in neuroimaging studies of depression. Neuropsychopharmacol *46*, 1510–1517. https://doi.org/10.1038/s41386-021-01020-7.

63. Kumari, R., Goel, S., and Das, S. (2022). Using SVM for Alzheimer's Disease detection from 3D T1MRI. In 2022 IEEE 21st Mediterranean Electrotechnical Conference (MELECON), pp. 600–604. https://doi.org/10.1109/MELECON53508.2022.9842935.

64. Johnson, P., Vandewater, L., Wilson, W., Maruff, P., Savage, G., Graham, P., Macaulay, L.S., Ellis, K.A., Szoeke, C., Martins, R.N., et al. (2014). Genetic algorithm with logistic regression for prediction of progression to Alzheimer's disease. BMC Bioinf. *15*, S11. https://doi.org/10.1186/1471-2105-15-S16-S11.

65. Gandhi, S., Khan, D., and Solanki, V.S. (2012). A Comparative Analysis of Selection Scheme. *2*, 4.

STAR★METHODS

KEY RESOURCES TABLE

REAGENT or RESOURCE	SOURCE	IDENTIFIER
Chemicals, peptides, and recombinant proteins		
[^{11}C]Martinostat PET radiotracer	Athinoula A. Martinos Center for Biomedical Imaging, Massachusetts General Hospital	https://www.martinos.org/core-services/positron-emission-tomography/
Deposited data		
SUVR data	This manuscript	Table S1
Software and algorithms		
Python	Python Software Foundation	https://www.python.org
Scikit-learn	Scikit-learn (Python library)	scikit-learn (RRID:SCR_002577) https://scikit-learn.org/stable/
Genetic Algorithm	Scikit-learn (Python library)	N/A
Support vector machine	Scikit-learn (Python library)	N/A
FreeSurfer	http://surfer.nmr.mgh.harvard.edu/	RRID:SCR_001847
FSL	http://www.fmrib.ox.ac.uk/fsl/	RRID:SCR_002823
Brain PET Data Reconstruction	https://surfer.nmr.mgh.harvard.edu/fswiki/BrainPET	https://surfer.nmr.mgh.harvard.edu/fswiki/BrainPET
Other		
Siemens head only PET/MRI scanner	Siemens Medical Solutions	N/A

RESOURCE AVAILABILITY

Lead contact

Requests for further information or resources should be directed to the lead contact, Changning Wang (cwang15@mgh.harvard.edu).

Materials availability

[^{11}C]Martinostat PET radiotracer was synthesized during this study. Availability is restricted,e.g. requiring a Material Transfer Agreement.

Data and code availability

- Data: The quantified and generated data of [^{11}C]Martinostat PET radiotracer regional brain relative tissue uptake values (SUVR$_{WB}$ and SUVR$_{pons}$) used for ML training and testing, of the 100 brain regions for AUD and CNT subjects (mean $\pm$ std) are available in Table S1. All data generated and/or analyzed reported in this paper will be shared by the lead contact upon request.
- Code: This paper does not report original code.
- Additional information: Any additional information required to reanalyze the data reported in this paper is available from the lead contact upon request.

EXPERIMENTAL MODEL AND STUDY PARTICIPANT DETAILS

Study design

Our research objective of this proof-of-concept study was to measure and compare *in vivo* HDAC expression in the brain between subjects with AUD and group-matched healthy controls (CNT) using [^{11}C]Martinostat PET-MR neuroimaging. Furthermore, we establish validation of a machine learning PET neuroimaging classification pipeline to assess the biomarker capability of the regional brain [^{11}C]Martinostat standard uptake values (SUV) in detecting individual subjects with AUD. SUV collected 60–90 minutes after radiotracer injection, normalized to whole brain mean (SUVR$_{WB}$), was the primary endpoint assessed. This study was approved by the Massachusetts General Brigham Institutional Review Board (IRB) and the Massachusetts General Hospital (MGH) Radioactive Drug Research Committee. All participants provided written informed consent according to the Declaration of Helsinki. Participants underwent a physical examination and a medical history review by a licensed study physician or nurse practitioner to determine study eligibility. Both participants with AUD and age- and sex-matched healthy controls (CNT) completed a [^{11}C]Martinostat simultaneous PET-MRI scan at the Athinoula A. Martinos Center for Biomedical Imaging to

determine brain uptake of [^{11}C]Martinostat and obtain specific neuroanatomical data. Imaging studies were not blinded to diagnosis, and no outliers were excluded.

Study approval

This study was approved by the Massachusetts General Brigham Institutional Review Board (IRB) and the Massachusetts General Hospital (MGH) Radioactive Drug Research Committee IRB protocol 2016P001398. All participants provided written informed consent according to the Declaration of Helsinki. AUD patients were recruited through Mclean hospital / Harvard Medical School, Division of Alcohol, Drugs, and Addiction. Imaging procedures were performed at the Athinoula A. Martinos Center for Biomedical Imaging. No adverse events were reported.

Study participants

Eleven patients with AUD and 16 healthy controls were matched for age and sex. All eligible participants were between the ages of 18 and 65 (Table 6), and were able to read, speak, and understand English. For participants with AUD, inclusion criteria included a DSM-5 diagnosis of alcohol use disorder, severe, according to the M.I.N.I. international neuropsychiatric interview and were abstinent from alcohol at least 4 days prior to the imaging scan without any signs of alcohol withdrawal at the time of the study physical examination. Data were collected between January 2017 and December 2022.

METHOD DETAILS

Radiosynthesis of [^{11}C]Martinostat

[^{11}C]Martinostat is the first ever PET radiotracer to selectively target class I HDAC enzymes in the *in vivo* human brain, developed by our group. Currently, it is the only PET imaging probing radiotracer agent available to be used with PET/MR imaging to visualize, map, and quantify class I HDAC enzymes regional brain expression density. [^{11}C]Martinostat is a hydroxamic acid-based HDAC inhibitor that contains an adamantyl group radiolabeled with ^{11}C. [^{11}C]Martinostat was synthesized through reductive alkylation, then by conversion into a hydroxamic acid in the presence of hydroxylamine and sodium hydroxide. This procedure was compliant with the cGMP guidelines.[20,21]

PET/MRI data acquisition

[^{11}C]Martinostat was injected through an intravenous catheter in the antecubital vein by a licensed nuclear medicine technologist. PET-MR scans were acquired simultaneously by using a 3T Siemens TIM Trio with a BrainPET insert. List-mode PET data spanning 0-90 minutes post-injection were collected. The intrinsic spatial resolution of PET in the center field of view (FOV) was < 3 mm.[49] An 8-channel head coil was used for the MR scanning. High-resolution T1-weighted anatomical scan was acquired with multi-echo magnetization prepared rapid acquisition gradient echo (MEMPRAGE) with prospective motion correction (using EPI-based volumetric navigators, vNavs), and the following parameters: repetition time (TR) = 2530 ms; echo times (TEs) = 1.66/3.53/5.4/7.27 ms; FOV = 280 mm; flip angle = 7 deg; voxel size =1 mm isotropic.[50]

MRI data processing and analysis

The MEMPRAGE images were segmented using FreeSurfer's automated segmentation and parcellation (version 6.0; http://surfer.nmr.mgh.harvard.edu/) based on the Desikan-Killiany atlas. The regions of interest (ROI) in native space were defined using these segmentations.

PET data reconstruction and analysis

PET images were reconstructed using the 3D Ordinary Poisson Ordered Subset Expectation Maximization algorithm from prompt coincidences, corrected for normalization, dead time, isotope decay, photon attenuation, and expected random and scatter coincidences. MR-based attenuation correction was applied using Statistical Parametric Mapping (SPM)–based, pseudo–computed tomography.[51] PET data spanning 60 to 90 min post radiotracer injection were binned into 6 bins containing 5 minutes each and reconstructed in units of $SUV_{60-90min}$ in 1.25 mm isotropic voxel size.[52] The $SUV_{60-90min}$ map was then normalized by a reference region, the whole brain $SUV_{60-90min}$ value,[26] generating $SUVR_{WB}$ maps for each subject. The region-based analysis was performed to quantify differences in [^{11}C]Martinostat uptake between AUD and controls. To account for the partial volume effects, especially for small size brain regions, and possible PET signal spillover from neighboring tissue, we applied geometric transfer matrix (GTM), a region-based partial volume correction (PVC) method using PETSurfer tools available within Freesurfer. The $SUVR_{WB}$ values were extracted from the regions in native space. Furthermore, to comprehensively interrogate *in vivo* HDAC expression in AUD, we also conducted voxel-wise analyses by registering individual $SUVR_{WB}$ images to the MNI standard space and smoothing it with a 6 mm Gaussian kernel.

Biomarker identification

Identifying reliable biomarkers is vital for effective diagnosis and selection of high efficacy treatments. With the current trend towards precision medicine, computational approaches are effective ways to detect biomarkers. Two relevant approaches come to the forefront: group difference analysis and single subject classification,[53] in one or more brain features. While group difference analysis gives insight into biological differences among control and patient groups which can inform diagnostic biomarkers, this analysis alone is not conclusive enough to be

used for precision diagnosis. The success of such approach is usually measured by the means of p-values. In single-subject classification, however, the objective is to accurately classify each subject into either the patient group or the control group by leveraging machine learning analysis. This approach is useful and can be easily implemented in clinical application for precision medicine as it has the capability to do inference in single individuals based on a trained machine learning model. The success of this approach is evaluated by classification metrics such as accuracy. Authors in this study[53] illustrated the possible scenarios that significant group differences do not necessarily cause high classification and vice versa. Taking this into consideration, we tested both methods; Voxel-wise group difference analysis and machine learning-based single subject classification.

Voxel-wise group difference analysis

Voxel-wise group difference analysis was performed using FSL (FMRIB software library, Oxford, UK; https://fsl.fmrib.ox.ac.uk/fsl/). A whole brain voxel-wise group comparison of $SUVR_{WB}$ between AUD patients and controls was conducted using FSL's FEAT with an unpaired *t*-test, ordinary least squares (OLS) mixed-effects modeling, a significance threshold of Z > 2.3, and cluster correction of $p_{cluster} < 0.05$.[54]

Machine learning based single subject classification analysis

The machine learning analysis is implemented to achieve precision AUD neuro-epigenetic detection/diagnosis. The implementation is done with Python and Sklearn package. In this proof-of-concept study, we examined 100 brain regions (including cortical and subcortical regions, listed in Table S1) to find out which region combination has the most classification or diagnostic or differentiation power. The $SUVR_{WB}$ features extracted from 100 regions are z-score normalized. We employed the so-called genetic algorithm, an advanced heuristic and machine learning based feature selection method. Feature selection methods help in identifying which independent variables (biological features) have a key role in influencing the dependent variable (diagnosis output). Next, the training and testing is carried out with leave-one-out (LOO) cross validation approach. We confirmed there was no anatomical bias that could influence the classification process (see Figures S11 – S14 where there is no significant brain region volume and thickness difference among AUD and Control class). After identifying the relevant brain regions that yield highest classification, we validate it by applying a support vector machine (SVM) ML classification algorithm.

Classification. Considering the small dataset we have, we utilized the popular SVMs classifier which is a supervised learning method for classification and regression.[55] Machine learning approaches such as SVMs are used in a wide range of brain imaging data for classification and diagnosis as well as biomarker identification.[56–63] In SVM, *n* numeric covariates in the dataset form an n-dimensional space and a hyperplane is selected for separation of points from different class. The distance between the hyperplane and the nearest data points on each side is called the margin. The hyperplane with the largest margin is preferred and referred to as Maximal-Margin hyperplane (Maximal-Margin Classifier). Those closest points are the support vectors as they define the hyperplane. However, the data in real world practice usually cannot be perfectly separated by a linear hyperplane in that space. Hence, the soft margin classifier is introduced, which allows some data points to violate the separating plane. The tuning parameter *C* defines the amount of violation allowed across all dimensions. In this case, the support vectors are the instances within the margin. To further deal with the non-linear separability, kernel functions inside SVM are introduced to perform non-linear transform and map finite-dimensional space into a space with much higher dimensions for better separation. The SVM algorithm is implemented by application of a radial kernel basis function. In prediction, the kernel defines a distance measure between new input and the support vectors. In linear SVM, the dot product is the measure of similarity as the distance is a linear combination of the inputs, which can be replaced by kernel function. Mathematically, the goal is to optimize the following objective function:

$$\min \omega(\alpha) = \frac{1}{2} \sum_{i=1}^{m} \sum_{j=1}^{m} y_i y_j \alpha_i \alpha_j \cdot K(x_i, x_j) - \frac{C}{2} \sum_{j=1}^{m} \alpha_j$$

$$s.t. \sum_{i=1}^{m} y_i \cdot \alpha_i = 0, 0 \leq \alpha_i \leq c$$

where $K(x, z) = \langle \varphi(x), \varphi(z) \rangle$ is a kernel function.

The Lagrangian is solved by Dual problem under the Karush-Kuhn-Tucker (KKT) condition. The optimal Lagrange multipliers are denoted as $\alpha^* = (\alpha_1^*, \alpha_2^*, ..., \alpha_m^*)^T$. The optimal solution is:

$$b^* = y_j - \sum_{i=1}^{m} y_i \alpha_i^* K(x_i, x_j)$$

$$f(x) = sign\left(\sum_{i=1}^{m} y_i \alpha_i^* K(x_i, x_j) + b^* \right)$$

Feature selection. We implement a model-based genetic algorithm for feature selection as depicted in Figure 6A. Model-based genetic algorithm (MGA) is an evolutionary approach used for relevant feature selection. Three important concepts in MGA include initial population,

fitness function and operators. The features selected by the MGA search are used as the input for machine learning models (i.e., support vector machine). The MGA uses the results from the models with different variable sets to perform an optimization and identify the best feature set. The MGA has been shown to perform feature selection significantly better than sequential variable selection methods or random subset selection. The initial population of potential solutions are randomly generated. The selection of individuals for mating is done using the tournament selection as used in Johnson, P. et al.[64] This method helps minimize early convergence of the algorithm, which often produces poor solutions. The tournament selection allows for easy adjustment of selection pressure by selection of tournament size to help tune the algorithm.[65] The tournament selection was performed by taking a random sample from the population of the given tournament size. This individual was used to select one parent by selecting the genome with the highest fitness. This sampling was then performed for the second parent, where the first parent could not be re-selected.

Uniform crossover is chosen for the reproduction of the next generation, noted as an optimal form of crossover for binary MGAs in Johnson, P. et al.[64] This involves the random swapping of chromosomes between parents to produce offspring with an assigned probability. For each crossover, two new individuals for the next generation are created, as depicted in Figure 6B.

The type of mutation chosen for the MGA algorithm implementation is a bit-flip mutation. This is chosen to prevent large changes to the binary genome. Large changes are more likely to result in instability and most often result in a less fit solution after the mutation operation. The mutation operation was performed by randomly selecting a few bits of the genome and flipping it. An example of a single-point mutation is shown in Figure 6C.

We used the following parameters: Initial population = 100, Mutation rate = 10%, Crossover rate = 90%, Tournament size = 2, Number of generations = 100, Max chromosome size = 100. With this size, there are 2^{100} combinations of genes. Accuracy measurement from the SVM model inside the MGA was used as a fitness value. The parameters were selected empirically. 10% mutation rate and 90% crossover rate are commonly used parameters in the literature of relevant feature selection in the context of medical diagnosis and prognosis.[64]

Terminology equivalence

Equivalent terminologies under genetic algorithm, machine learning and our AUD neuroepigenetics framework (Figure 6D) is described in Table 7.

QUANTIFICATION AND STATISTICAL ANALYSIS

Machine learning classification evaluation metrics for biomarker validation

To validate the classification performance for binary classes (i.e., AUD vs. CNT), we constructed a 2 × 2 contingency table (confusion matrix), as shown in Table 8. We used these ML classification performance evaluation metrics to validate the reliability of the identified potential neuro-epigenetic biomarkers (i.e., [^{11}C]Martinostat uptake (SUVR$_{WB}$)) in differentiating AUD patients from control subjects.

True Positive (TP): Number of observations that are correctly classified as "AUD" group.
True Negative (TN): Number of observations that are correctly classified as "control" group.
False Positive (FP): Number of observations that are incorrectly classified as "AUD" group.
False Negative (FN): Number of observations that are incorrectly classified as "control" group.
Accuracy (ACC): Accuracy measures the overlap between the ML algorithm classification outcome and the clinical diagnosis.

$$ACC = (TP + TN) / (TP + TN + FP + FN)$$

(Worst value: 0; best value: 100%)
Sensitivity (SENS) & specificity (SPEC): Sensitivity measures the proportion of "AUD" that are correctly classified, while specificity measures the proportion of "controls" that are correctly identified:

$$SENS = \frac{TP}{TP+FN}, SPEC = \frac{TN}{TN+FP}$$

(Worst value: 0; best value: 100%)
Positive Predictive Value (PPV) & Negative Predictive Value (NPV): PPV measures the proportion of true "AUD" observations among predicted "AUD" observations. Similarly, NPV measures the proportion of true "control" observations among predicted "No-Response" observations:

$$PPV = \frac{TP}{TP+FP}, NPV = \frac{TN}{TN+FN}$$

(Worst value: 0; best value: 100%)
AUC (area under ROC curve): AUC measures the degree of separability between classes at various threshold settings and is obtained by calculating the area under the receiver operating characteristic (ROC) curve.

(Worst value: 0; best value: 1)

F1 score: F1 score measures the harmonic mean of the precision: i.e., out of all the examples that are predicted as positive, how many are true positives? and recall: i.e., out of all the positive examples, how many are predicted as positive? It performs well on an imbalanced class dataset.

$$\text{F1} = \frac{TP}{TP + \frac{1}{2}(FP+FN)}$$

(Worst value: 0; best value: 100%)

Matthews correlation coefficient (MCC): MCC is a more reliable statistical rate that produces a high score only if the prediction/classification obtained good results in all of the four confusion matrix categories (true positives, false negatives, true negatives, and false positives), proportional both to the size of positive elements and the size of negative elements in the dataset.

$$\text{MCC} = \frac{TP.TN - FP.FN}{\sqrt{(TP+FP).(TP+FN).(TN+FP).(TN+FN)}}$$

(Worst value: –1; best value: +1)

Cohen's Kappa (CK): CK measures inter-rater agreement where the actual class category and the predicted classes are considered as two different raters.

$$CK = \frac{Po - Pe}{1 - Pe}$$

where p_0 is the overall accuracy of the model and p_e is the measure of the agreement between the model predictions and the actual class values as if happening by chance.

(Worst value: -1; best value: +1)

Statistics: For whole brain voxel-wise SUVR$_{WB}$ comparisons between groups, an unpaired 2-tailed t test was performed with Z > 2.3 and P$_{cluster}$ < 0.05 correction (Figure 1A and Table 1). For the post hoc ROI SUVR$_{WB}$ comparison between groups, Wilcoxon rank-sum test was used to assess between group differences (Figure 1C). A leave-one-out (LOO) cross validated F1 score, Accuracy, AUC, Sensitivity, Specificity, PPV, NPV, MCC and CK classifications metrics are reported for the given machine learning classification settings (Figure 2, Figure S2-S10, Table 4). Since LOO classification results are deterministic, mean ± SD results are not reported. Genetic algorithm feature selection was performed and as a fitness value, classification accuracy with confidence interval is reported for the final selected features in each generation (Figure 3A). Area under the ROC curve was computed (Figure 4, Table 4). Pair-wise Pearson's correlation was computed among the identified SUVR$_{WB}$ features (Figure 5B, Table 5) and the correlogram of the identified 5 brain region SUVR$_{WB}$ biomarkers in each group is computed using Python and visualized with Seaborn package. The relative [^{11}C]Martinostat uptake values (i.e., SUVR$_{WB}$) in the selected brain regions (i.e., identified neuro-epigenetics HDAC biomarker regions) in AUD and control groups were summarized as the mean ± SD (Table 2). Confusion matrix is computed for the SVM classification using the SUVR$_{WB}$ features of the identified brain regions HDAC biomarkers (Table 3). Study Participant's demographic information were summarized as the mean ± SD (Table 6). SUVR$_{WB}$ and SUVR$_{PONS}$ of 100 brain regions in AUD patients and CNT subjects were summarized as the mean ± SD (Table S1). The Mann-Whitney statistical test is used to compare regional HDAC expression desnsity and the brain regions volume and thickness between AUD patients and control subjects (Figures S1 and S11-S14).